Theoretical study of Nb isotope productions by muon capture reaction on ^{100}Mo

Maureen Ciccarelli,[1,2] Futoshi Minato,[1,*] and Tomoya Naito[3,4,†]
[1]*Nuclear Data Center, Japan Atomic Energy Agency, Tokai, Ibaraki 319-1195, Japan*
[2]*Université de Lille, 59000 Lille, France*
[3]*Department of Physics, Graduate School of Science, The University of Tokyo, Tokyo 113-0033, Japan*
[4]*RIKEN Nishina Center, Wako 351-0198, Japan*

(Received 11 November 2019; revised 16 May 2020; accepted 18 August 2020; published 3 September 2020)

Background: The isotope ^{99}Mo, the generator of ^{99m}Tc used for diagnostic imaging, is supplied by extraction from fission fragments of highly enriched uranium in reactors. However, a reactor-free production method of ^{99}Mo is sought worldwide due to concerns about nuclear proliferation.
Purpose: Production methods using accelerators have attracted attention. Recently, ^{99}Mo production through a muon capture reaction was proposed and it was found that about 50% of ^{100}Mo turned into ^{99}Mo through the ^{100}Mo (μ^-, n) reaction [I. Hashim *et al.*, Nucl. Instrum. Methods Phys. Res., Sect. A **963**, 163749 (2020)]. However, the detailed physical process of the muon capture reaction is not completely understood. We therefore study the muon capture reaction on ^{100}Mo by a theoretical approach.
Methods: We use the proton-neutron quasiparticle random phase approximation to calculate the muon capture rate. The muon wave function is calculated with consideration of the electronic distribution of the atom and the nuclear charge distribution. The particle evaporation process from the daughter nucleus, ^{100}Nb, is calculated by the Hauser-Feshbach statistical model.
Results: From the model calculation, about 38% of ^{100}Mo is converted to ^{99}Mo through the muon capture reaction, which is in reasonable agreement with the experimental data. It is revealed that negative parity states, especially the 1^- state, play an important role in ^{100}Mo (μ^-, n) ^{99}Nb. Charged particle emission is hindered due to its large separation energy and the Coulomb barrier.
Conclusions: Isotope production by the muon capture reaction strongly depends on the nuclear structure. To understand the mechanism, excitation energy functions have to be known microscopically.

DOI: 10.1103/PhysRevC.102.034306

I. INTRODUCTION

The isotope ^{99}Mo ($T_{1/2} = 66$ h) is used as the generator of ^{99m}Tc, which is the most widely used radioisotope for medical diagnostic imaging in the world [1]. Currently, most ^{99}Mo is produced by fission reactions of highly enriched ^{235}U (HEU) or low enriched ^{235}U in nuclear reactors in some countries [2]. However, the HEU is an issue of public concern in terms of nuclear proliferation, and a special regulation to deal with it obstructs the global expansion of production locations. Also, some of the reactors producing ^{99}Mo have been operated for more than 40 years since they were launched. A discussion about the decommissioning of those reactors could happen at any time. In fact, the National Research Universal (NRU) reactor at Chalk River in Canada, which had produced about 40% of the world supply before, began to shut down in 2018.

For those reasons, an alternative reactor-free production method of ^{99}Mo is sought in order to sustain its stable supply. A production method using accelerators is a promising candidate and has attracted attention. Several methods through charged particle reactions, such as ^{100}Mo(p, pn) ^{99}Mo, ^{100}Mo $(d, p2n)$ ^{99}Mo, and ^{100}Mo $(p, 2n)$ ^{99}Tc, and photodisintegration reactions, such as ^{238}U (γ, f) ^{99}Mo and ^{100}Mo (γ, n) ^{99}Mo [3–6], have been proposed. In addition to the above reactions, it is also proposed to use high-energy neutrons produced by accelerators [7,8], which are suitable to produce ^{99}Mo through the ^{100}Mo $(n, 2n)$ ^{99}Mo reaction [9,10].

It is also possible to produce ^{99}Mo by using a negative-muon capture reaction (hereafter, we call it simply muon capture). In this approach, ^{99}Mo is generated through the β^- decay of ^{99}Nb, which is produced by the ^{100}Mo (μ^-, n) ^{99}Nb reaction. Muon capture has several advantages in ^{99}Mo productions as compared to the aforementioned approaches. First, it makes the best use of a muon resource because muons rapidly lose kinetic energy in a target material and form muonic atoms with a high probability of capture by one of the orbitals of an atom [11]. Second, muon capture deposits in a target nucleus a high energy of about 10–20 MeV on average [12–14], which is suitable to emit only a few neutrons, avoiding production of unnecessary isotopes. Third, target samples can be reused efficiently because the muon capture changes the atomic number of a nucleus by only 1, and if the daughter nucleus is unstable it decays back to the original atomic number. This point is also important to suppress the impurities of unnecessary isotopes.

*minato.futoshi@jaea.go.jp
†tomoya.naito@riken.jp

Recently, Nb isotope mass distributions by ^{100}Mo $(\mu^-, xn)^{100-x}$Nb [15] and $^{\rm nat}$Mo$(\mu^-, xn)^{100-x}$Nb [16,17] were studied experimentally at MUSE in the J-PARC Material Life Science Facility (MLF) and MuSIC in Osaka University, respectively, where it was shown that about 50% of ^{100}Mo turned into ^{99}Nb and more than 45% into unstable Nb isotopes which become Mo isotopes eventually by β^- decay. In addition, it was observed that charged particle emissions were strongly hindered. This fact indicates that the muon capture is a potential candidate for ^{99}Mo production if a high-flux muon beam could be obtained.

In spite of the above experimental measurements, the muon capture reaction is not perfectly understood from the theoretical point of view. In particular, it is still not clear why the ^{100}Mo (μ^-, n) ^{99}Nb reaction occurs with such high probability. The Nb isotope mass distribution was discussed in Refs. [15,16] using a preequilibrium and equilibrium (proton) neutron emission model [18], which gave good agreement with the experimental data. However, the model used phenomenological functions for excitation energies of the daughter nucleus, and they could not discuss the details of muon capture reaction in terms of the nuclear structure microscopically. To disentangle the physical processes of the muon capture reaction on Mo isotopes, a microscopic analysis is needed. The muon capture reaction on ^{100}Mo was also investigated recently by the proton-neutron quasiparticle random phase approximation (*pn*-QRPA) [19]. However, they only discussed the capture rate and not the neutron evaporation process.

The aim of this work is to understand further details on the muon capture reactions on Mo isotopes from the nuclear structure point of view. To this end, the *pn*-QRPA is used in this work as in Ref. [19], on the basis of the Skyrme-Hartree-Fock + BCS model (SHFBCS) [20] for the muon capture. For the particle evaporation steps, we adopt the Hauser-Feshbach statistical model (HFSM) [21], which properly considers the energy conservation, the selection rule based on the nuclear structure, the transmission probabilities of emitted particles, and so on. The *pn*-QRPA is able to cover a wide range of nuclei and has been used for a systematical calculation of muon capture across the nuclear chart [22–25]. For our future plan to make a new table of muon capture reactions, the *pn*-QRPA is thus adopted in our work. We would like to stress that the nuclear axial deformation is taken into account in our model. We also consider effects of the electron distribution, as well as the nuclear finite size, on the muon wave function and its eigenenergy, i.e., binding energy.

This paper is organized as follows. In Sec. II, the theoretical framework used in this work is described. In Sec. III, results of the muon capture reaction on ^{100}Mo and other Mo isotopes are given, and details about the nuclear structure effects on the muon capture reaction are discussed. We summarize this work in Sec. IV.

II. THEORETICAL FRAMEWORK

The muon capture reaction undergoes two steps, that is to say, the ground-state target nucleus i is transmuted to a highly excited state f of the daughter nucleus by the muon capture and the highly excited daughter nucleus f evaporates particles and is transmuted to the residual nucleus r. During the former process, the muon is assumed to be captured in its $1s$ orbital.

The muon capture rate in the former process, ω_{fi}, is calculated from the *pn*-QRPA, and the ratio of the residual nucleus r after the latter process, $P^{\rm emit}_{rf}$, is calculated from the HFSM. Here, the muon wave function before the muon capture has to be considered properly. Finally, isotope production rates by the muon capture reaction are given by

$$P_r = \frac{\sum_f \omega_{fi} P^{\rm emit}_{rf}}{\sum_f \omega_{fi}}. \tag{1}$$

We will describe the framework to compute ω_{fi}, $P^{\rm emit}_{rf}$, and the muon wave function in the following subsections.

A. Muon capture rate

The muon capture rate is given by [26,27]

$$\omega_{fi} = \frac{2G^2\nu^2}{1+\nu/M_{\rm T}} \frac{1}{2J_i+1} \times \sum_{M_i M_f} \left\{ \sum_{JM} |\langle J_f M_f | \phi_{1s} (\hat{\mathcal{M}}_{JM} - \hat{\mathcal{L}}_{JM}) | J_i M_i \rangle|^2 + \sum_{JM} \left| \langle J_f M_f | \phi_{1s} \left(\hat{\mathcal{T}}^{\rm el}_{JM} - \hat{\mathcal{T}}^{\rm mag}_{JM} \right) \right| J_i M_i \rangle \right|^2 \right\}, \tag{2}$$

where $G = 1.166 \times 10^{-11}$ MeV^{-2} [28] is the Fermi coupling constant, $M_{\rm T}$ is the mass of the target nucleus, ν is the muon neutrino energy, and $\phi_{1s} \equiv \phi_{1s}(\vec{r})$ is the muon wave function of the $1s$ orbital. In this work, we restrict ourselves to study only Mo isotopes with even mass number for simplicity of numerical calculation, and thus we set $J_i = 0$. The definitions of the Coulomb and longitudinal multipole operators, $\hat{\mathcal{M}}_{JM}$ and $\hat{\mathcal{L}}_{JM}$, and the transverse electric and magnetic multipole operators, $\hat{\mathcal{T}}^{\rm el}_{JM}$ and $\hat{\mathcal{T}}^{\rm mag}_{JM}$, in Eq. (2) are given in Refs. [25,27], where J and M satisfy $\vec{J}_f = \vec{J}_i + \vec{J}$ and $M_f = M_i + M$, respectively. From the energy conservation [14,25],

$$m_\mu + \varepsilon_b + E_i = E_f + \nu, \tag{3}$$

where m_μ is the muon mass, $\varepsilon_b < 0$ is the binding energy of the muon, and E_i and E_f are the energies of initial and final states. We approximate $E_f - E_i = m_n - m_p + (\lambda_n - \lambda_p + E_{\rm QRPA})$ [29,30], where m_n and m_p are the neutron and proton masses, λ_n and λ_p are the neutron and proton Fermi energies of the initial nucleus, and $E_{\rm QRPA}$ is the eigenvalue of the *pn*-QRPA equation [30]. We use the effective axial-vector coupling constant $g_{\rm A} = 1$, instead of the free-nucleon one $g_{\rm A} = 1.26$, in the multipole operators.

1. SHFBCS and pn-QRPA

To calculate the transition matrix elements appearing in the curly braces of Eq. (2), the *pn*-QRPA is used in this work.

First, the ground state of the initial nucleus, $|J_i M_i\rangle$, is calculated by the SHFBCS [20] with the SLy4 effective interaction [31]. We consider the axial deformation of the nucleus assuming reflection symmetry. The mesh sizes for

numerical calculations are $\Delta\rho = \Delta z = 0.8$ fm and the box boundary conditions are $\rho_{\max} = z_{\max} = 16$ fm. In the BCS approximation, the volume-type pairing force is used for the isospin $T = 1$ channel, and the neutron and proton pairing strengths are set to be $V_n = 286.669$ and $V_p = 295.369$ MeV [32], respectively. The pairing active space is chosen in the same way as in Ref. [32]. We do not take into account the isospin $T = 0$ pairing both for the ground and excited states because its effect is small. Under these conditions, we obtain $\beta_2 = 0.21$ for ^{100}Mo and $\beta_2 \simeq 0.00$ for the other Mo isotopes. Note that although there are plenty of theoretical studies on charge-changing transitions, the β^+ transition extending to a high excitation energy region as the negative muon capture is still not well established. In particular, time-odd components of the Skyrme effective interaction, which sensitively influence spin-multipole transitions, are not understood well, although important progress has been made [33–36]. In this respect, this work is challenging; however, we expect that we will be able to obtain some hints to constrain the time-odd components of the Skyrme force from the muon capture reaction.

Next, the matrix elements appearing in Eq. (2) are calculated by using the *pn*-QRPA. The *pn*-QRPA calculation is performed by the diagonalization approach [30]. The residual interaction is fully taken into account, being consistent with the ground-state calculation of the SHFBCS. The transition matrix elements of Eq. (2) are thus calculated as

$$|\langle J_f M_f|\hat{\mathcal{O}}_{JM}|J_i M_i\rangle|^2 = \left|\sum_{np}(\langle n|\hat{\mathcal{O}}_{JM}|\bar{p}\rangle X_{np}u_n v_p - \langle \bar{n}|\hat{\mathcal{O}}_{JM}|p\rangle Y_{np}u_p v_n)\right|^2. \quad (4)$$

The ket states in Eq. (4) of $|p\rangle$ and $|n\rangle$ correspond to the single-particle states of protons and neutrons, respectively, and $|\bar{p}\rangle$ and $|\bar{n}\rangle$ are their time-reversed states. The coefficients X_{np} and Y_{np} are the forward and backward amplitudes of the *pn*-QRPA, respectively, and u_i and v_i are the BCS coefficients [30]. The operator $\hat{\mathcal{O}}_{JM}$ is any of the multipole operators in Eq. (2). Here, we include single-particle levels up to 30 MeV above the Fermi energies as the model space of the *pn*-QRPA.

The isoscalar ($T = 0$) pairing is essential to reproduce experimental β-decay half-lives [29,37] and would be relevant to muon capture rates. However, as mentioned above, we omitted the isoscalar pairing in this work because it is found that using no isoscalar pairing is more favorable to reproduce β-decay half-lives around ^{100}Nb systematically. For example, the calculated half-life of ^{100}Nb is $T_{1/2}^{\text{calc.}} = 4.1$ s in the present formalism (where we applied the same method as in even-even nuclei for the BCS occupation probabilities of ^{100}Nb), while $T_{1/2}^{\text{exp.}} = 1.5$ s. The gap between the calculated and experimental half-lives can be reduced if we slightly increase the isoscalar pairing strength in the particle-particle matrix element of *pn*-QRPA. However, the result of muon capture reaction remains unchanged qualitatively even if we include the isoscalar pairing, at lease in nuclei of interest in this work.

We define the mean excitation energy of a daughter nucleus after the muon capture as

$$\overline{E} = \sum_f \omega_{fi} E_f^*, \quad (5)$$

where $E_f^* = E_{\text{QRPA}} - E_{\text{2qp, lowest}}$ and $E_{\text{2qp, lowest}}$ is the sum of the lowest proton and neutron quasiparticle energies [29].

2. Muon wave function

The muon wave function is given by solving the Schrödinger or Dirac equation under the external potential V_{pot}, which is composed of two parts:

$$V_{\text{pot}}(r) = V_{\mu\text{-}N}(r) + V_{\mu\text{-}e}(r), \quad (6)$$

where the potential is assumed to have spherical symmetry.

The former one, $V_{\mu\text{-}N}$, is the Coulomb potential due to the nucleus. The charge distribution of the atomic nucleus ρ_{ch} is considered in $V_{\mu\text{-}N}$ and thus it is different from the simple potential $-Z/r$:

$$V_{\mu\text{-}N}(r) = -4\pi e^2 \int_0^r \frac{1}{r'^2}\int_0^{r'} \overline{\rho}_{\text{ch}}(r'')r''\,dr''\,dr', \quad (7)$$

where $\overline{\rho}_{\text{ch}}$ is the spherical-averaged charge distribution, that is,

$$\overline{\rho}_{\text{ch}}(r) = \frac{1}{4\pi}\int \rho_{\text{ch}}(\vec{r})\,d\Omega. \quad (8)$$

It should be noted that even if the nuclear charge distribution ρ_{ch} is deformed in the intrinsic frame, in general the spherical-averaged distribution $\overline{\rho}_{\text{ch}}$ should be used in Eq. (7), since the muon wave function is calculated in the laboratory frame.

To obtain the charge distribution of Mo isotopes, the proton density calculated by the SHFBCS is convoluted with the proton form factor as follows:

$$\rho_{\text{ch}}(\vec{r}) = \int \rho_p(\vec{r}')G(\vec{r}' - \vec{r})\,d\vec{r}', \quad (9)$$

where the function $G(\vec{r}) = (r_0\sqrt{\pi})^{-3}\exp(-\vec{r}^2/r_0^2)$ is the Fourier transformation of the electric form factor $G(q^2)$ of protons and ρ_p is the proton density distribution given by the SHFBCS. We assume the proton root-mean-square radius $\sqrt{\langle r_p^2\rangle} = 0.8414$ fm [28], which corresponds to $r_0 = 0.687$ fm. In this calculation, first the spherical-averaged proton density distribution $\overline{\rho}_p$ is calculated and it is substituted into Eq. (9) to obtain $\overline{\rho}_{\text{ch}}$.

In the practical calculation, to calculate Eq. (7), the calculated spherical-averaged charge density distribution $\overline{\rho}_{\text{ch}}$ is fitted to the Fourier-Bessel function [38],

$$\overline{\rho}_{\text{ch}}(r) = \begin{cases} \sum_{j=1}^{17} a_j j_0(j\pi r/R) & \text{for } r < R, \\ 0 & \text{for } r > R, \end{cases} \quad (10)$$

where

$$j_0(x) = \frac{\sin(x)}{x} \quad (11)$$

is the spherical Bessel function. The coefficients a_j are obtained by using GNUPLOT and R is determined as the minimum value of r which satisfies $\overline{\rho}_{\text{ch}}(r) < 10^{-6}$ fm^{-3}.

The latter one, $V_{\mu\text{-}e}$, is the Coulomb interaction between the muon and the electrons of the atom, which reads

$$V_{\mu\text{-}e}(r) = e^2 \int \frac{\rho_e(\vec{r})}{|\vec{r} - \vec{r}'|} d\vec{r}', \tag{12}$$

where ρ_e is the electron distribution.

In this work, the number of the electrons is assumed to be the same as the atomic number Z, i.e., the muon is captured by the neutral atoms. The number density of electrons ρ_e is calculated using density functional theory (DFT) in the Dirac scheme [39–41], performed by the calculation package "Atomic Density functional program PACKage" (ADPACK) [42], and it is assumed to be spherically symmetric. The Perdew-Zunger exchange-correlation functional in the local density approximation, as known as the "PZ81" functional [43], is used.

After V_{pot} is calculated, the muon wave function is calculated numerically within a uniform mesh of $\log r$.

B. Calculation of evaporation residue by HFSM

To describe the particle evaporation step, we used the HFSM module implemented in Comprehensive Code for Nuclear Data Evaluation (CCONE) developed in the Nuclear Data Center, JAEA [44]. We assume that the daughter nucleus reaches the compound state, soon after the muon capture and the particle evaporation follows the statistical process.

The following quantities of the compound nucleus are required to run the CCONE as inputs: (1) transmission coefficients of nucleons, deuteron, triton, and helium-3 calculated by Koning-Delaroche optical potentials [45] and folding potentials; (2) transmission coefficient of the α particle calculated from the optical potential of Avrigeanu [46]; (3) the enhanced generalized Lorentzian function of Kopecky-Uhl [47], which is used for the γ-strength function; (4) the Gilbert-Cameron method [48] with the Mengoni-Nakajima parameter [49], which is used for the nuclear level densities; and (5) masses taken from AME2016 [50,51] if available and FRDM12 [52] for otherwise.

The contribution from the preequilibrium process is nonnegligible in the particle evaporation after the muon capture [15,16,53]. In addition, it can be considered that the direct process also contributes particle emissions because the muon capture gives high enough energy to kick protons out of the nucleus directly. However, this work considers neither the preequilibrium nor direct processes, which are left for our future work.

III. RESULTS

A. Muon capture rate of $^{\text{nat}}$Mo

We first estimate the muon capture rates of Mo isotopes with even mass numbers to check if our theoretical framework works well. The calculated muon capture rates are listed in Table I with the natural abundance (NA) of Mo isotopes. Only experimental data of the muon capture rate of $^{\text{nat}}$Mo is available (see Ref. [54] and references therein). For ^{95}Mo (NA = 15.84%) and ^{97}Mo (NA = 9.5%), that are odd-A systems, we estimate the muon capture rates by taking an average of neighboring nuclei. The pn-QRPA gives $\omega_{fi} = 11.3 \times 10^6$ s^{-1} for $^{\text{nat}}$Mo, which reproduces the experimental data ($(9.614 \pm 0.15) \times 10^6$ s^{-1} [54]) with a deviation of about 15%. Assuming that the computed muon capture rate of ^{100}Mo is also overestimated by a deviation of 15%, the expected muon capture rate of ^{100}Mo is $\omega_{fi} = 8.34 \times 10^6$ s^{-1}. Compared to the muon decay rate ($\omega_{\text{weak}} = 4.552 \times 10^5$ s^{-1} [55]), the muon capture on the nucleus occurs much faster than the muon weak decay ($\mu^- \to e^- + \overline{\nu}_e + \nu_\mu$). The ratio is calculated as $\omega_{fi}/(\omega_{fi} + H\omega_{\text{weak}}) \simeq 0.95$, where $H = 0.936$ is the Huff factor taken from Ref. [54].

TABLE I. Calculated muon capture rates and natural abundance (NA) of Mo isotopes with even masses. Experimental muon capture rate for natural Mo is also listed [54].

Nucleus	ω_{fi} (10^6 s^{-1})	NA (%)
^{92}Mo	13.3	14.53
^{94}Mo	12.2	9.15
^{96}Mo	11.3	16.67
^{98}Mo	10.3	24.39
^{100}Mo	9.8	9.82
$^{\text{nat}}$Mo (calc.)	11.3	
(exp.)	9.614 ± 0.15	

B. Muon capture reaction of ^{100}Mo

Figure 1 illustrates the muon capture rates of positive and negative parity states for the daughter nucleus ^{100}Nb as functions of excitation energy E^*. The curves shown are smoothed by a Lorentzian function with a width of 1 MeV. We also show the separation energies of one neutron ($S_n =$ 5.5 MeV), two neutrons ($S_{2n} = 11.1$ MeV), and three neutrons ($S_{3n} = 18.4$ MeV). The sums of negative and positive parities are indicated by the solid lines in the panels. We can see characteristic structures in the muon capture rates, which are different from the one estimated in Ref. [15]. Our result clearly indicates the importance of the nuclear structure effect on the muon capture. The present model does not give any strong strength distributions above 35 MeV for either negative or positive parity states.

It is clearly seen from Fig. 1 that the negative parity state distribution lies in the low energy region and its main component spreads in $E^* \leqslant S_{2n}$. On the other hand, the positive parity state distributon lies in a higher energy region than the negative parity and its main peaks appear above S_{2n}. This difference can be explained by considering the shell structure of ^{100}Nb. The numbers of nucleons of ^{100}Nb are close to submagic number $Z = 40$ and magic number $N = 50$, and thus proton and neutron pf shell and neutron intruder $1g$ states are almost occupied. Therefore, the negative parity states are usually populated by a transition from the proton pf shell to the neutron sdg shell, so that the transition energy required is around $1\hbar\omega$ if the Coulomb force is neglected. In fact, the first peak observed in $E^* < 5$ MeV for 1^- state is mainly due to the coherent transitions from the proton $1f_{5/2}$ state to the neutron $1g_{7/2}$ state and from the proton $2p_{3/2}$ state to the neutron $2d_{3/2}$ state, and the second peak is due to the

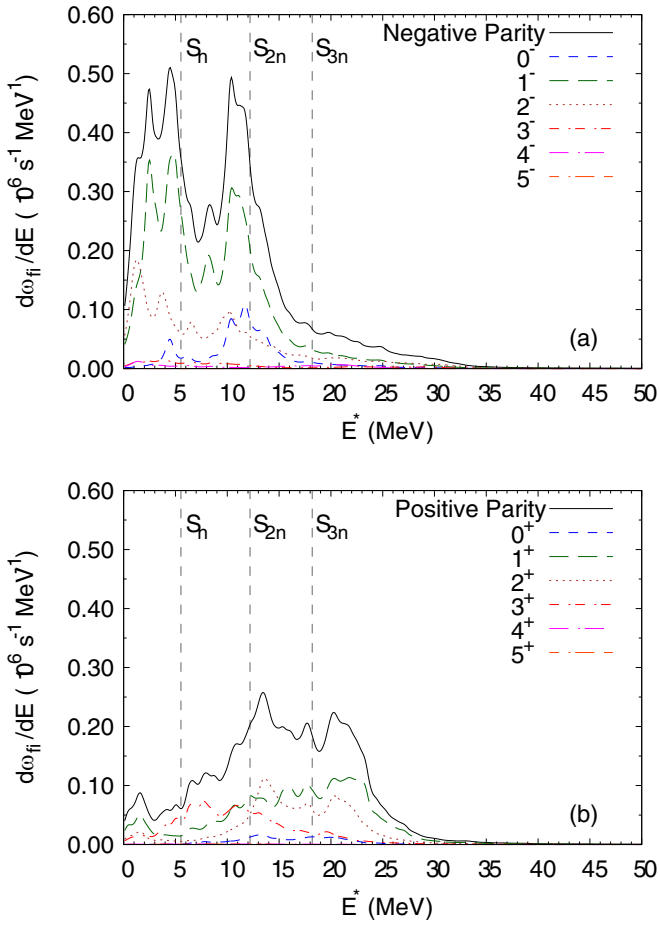

FIG. 1. Muon capture rates as a function of excitation energy for (a) negative parity and (b) positive parity states of ^{100}Nb. Neutron separation energies are indicated by the dotted lines.

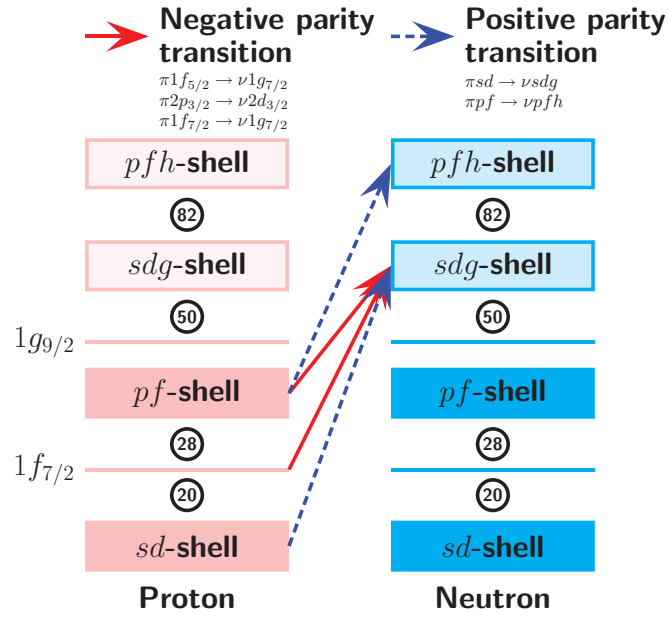

FIG. 2. Schematic figure of transitions. Red solid and blue dashed arrows correspond to negative and positive parity transitions, respectively. Shells with dark color represent almost occupied states and those with light color are unoccupied ones. Here, the Coulomb interaction is neglected for simplicity, and thus the energies of protons and neutrons are identical.

transition from the proton $1f_{7/2}$ state to the neutron $1g_{7/2}$ state, in the spherical picture. On the other hand, the positive parity states are mainly populated by a transition energy from the proton *sd* shell to the neutron *sdg* shell or from the proton *pf* shell to the neutron *pfh* shell, so that the transition energy required is around $2\hbar\omega$. Therefore, the negative parity state is more significant than the positive parity state in the low energy region, and it is considered that the negative parity state gives a large contribution to ^{100}Mo (μ^-, n) ^{99}Nb. This mechanism is schematically shown in Fig. 2.

From the calculated muon capture rates and excited states, particle evaporations are calculated by the HFSM. The obtained result of the Nb isotope mass distribution of the ^{100}Mo (μ^-, xn) reaction is listed in Table II. Considering our lack of knowledge on low-lying β^+-type transitions and uncertainties in spin-isospin transitions in the present theoretical model, the strength distributions of a daughter nucleus yielded by muon capture would not be reproduced correctly. In spite of that, it is remarkable that the present model reasonably reproduces the production rate of the muon capture reaction. Only for ^{100}Nb is the production rate rather overestimated. This overestimation comes from too many feedings to the excited states below S_n by the muon capture, and this can be observed in Fig. 1, especially for the negative parity state. We should keep in mind that the present theoretical model has the ambiguity seen in Table II. However, we believe that the qualitative discussion given in the following will not be affected by it.

Now, we try to demonstrate the reason why the ^{100}Mo (μ^-, n) ^{99}Nb reaction occurs with high probability using the present formalism. Figure 3 shows the production rate of Nb isotopes by the muon capture reaction for different spin-parity states. We did not show the contributions from $4^\pm$ and $5^\pm$ states because they are not significant. We can clearly see that the production rates of isotopes with large mass numbers are mainly due to negative parity states and those with small mass numbers are due to positive parity states. The production rates of ^{99}Nb and ^{100}Nb mainly come from the 1^- state as expected. The high probability of the ^{100}Mo (μ^-, n) ^{99}Nb

TABLE II. Production rate of Nb isotopes by the muon capture reaction on Mo isotopes (%). The experimental data are taken from Ref. [15]. Charged particle emission rate is also listed.

Reaction	Experiment	This work
^{100}Mo $(\mu^-, 0n)$ ^{100}Nb	8	28.9
^{100}Mo $(\mu^-, 1n)$ ^{99}Nb	51	38.1
^{100}Mo $(\mu^-, 2n)$ ^{98}Nb	16	23.8
^{100}Mo $(\mu^-, 3n)$ ^{97}Nb	13	8.73
^{100}Mo $(\mu^-, 4n)$ ^{96}Nb	6	0.28
^{100}Mo $(\mu^-, 5n)$ ^{95}Nb	3	0.01
Charged particle emission		0.06

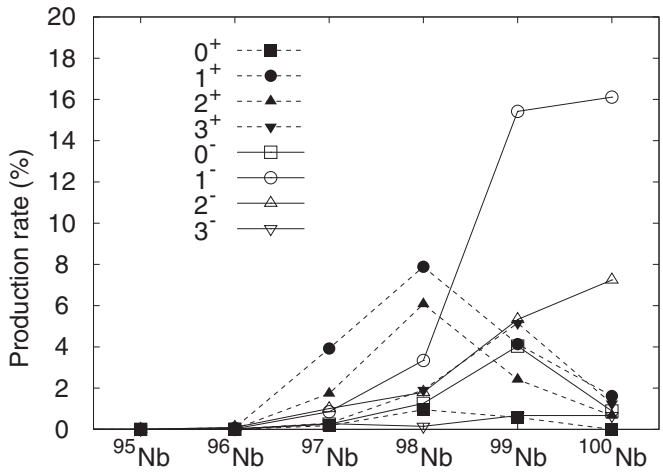

FIG. 3. Production rate of Nb isotopes by the muon capture reaction for different spin-parity states.

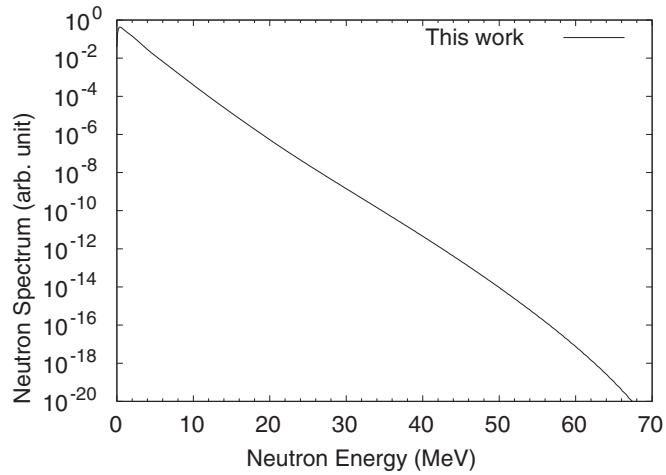

FIG. 5. Computed neutron spectrum for the ^{100}Mo(μ^-, xn) reaction. The curve is normalized arbitrarily.

reaction thus results from the nuclear structure of proton and neutron shells described above.

To qualitatively understand the isotope production rates of the muon capture reaction, we illustrate $\overline{E}$ and the muon capture rates for different spin-parity states in Fig. 4. The dashed, dotted, and long-dashed lines in panel (a) are S_n, S_{2n}, and one-proton separation energies ($S_p = 9.5$ MeV) of ^{100}Nb. The mean excitation energies of every state exceed the one-neutron separation energy, and ^{99}Nb is easy to produce.

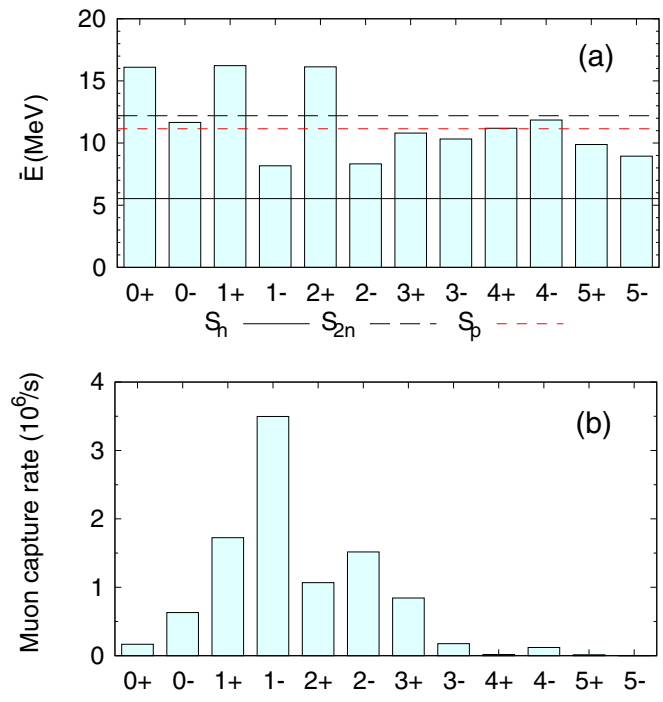

FIG. 4. (a) Mean excitation energy $\overline{E}$ for different spin-parity states. Separation energies of one and two neutrons, and one proton for ^{100}Nb are also shown by the black solid, dotted, and red dashed lines, respectively. (b) Muon capture rates on ^{100}Mo for different spin-parity states of ^{100}Nb.

Among $0^{\pm}$, $1^{\pm}$, and $2^{\pm}$ states, the positive parity states have larger mean excitation energies than the negative parity states as expected, and the mean excitation energies exceed S_{2n} for 0^+, 1^+, and 2^+ states.

Panel (b) of Fig. 4 shows the muon capture rate ω_{fi} of different spin-parity states of ^{100}Nb. Considering uncertainty arising from the axial-vector coupling constant, g_A, the capture rates of unnatural parities may change. However, it is expected that the overall shape of Fig. 4(b) does not change significantly. The 1^- and 2^- states have the largest and the third largest contributions. Their $\overline{E}$ values are below S_{2n} and S_p, and thus they easily evaporate one neutron and are transmuted to ^{99}Nb. The second largest contribution is the 1^+ state with $\overline{E} \simeq 16$ MeV, which is greater than S_{2n} and S_p, and thus it is transmuted to ^{99}Nb as well as ^{98}Nb and ^{100}Zr. The muon capture rates of 0^+ and 2^+ states are relatively small, contributing less to ^{99}Nb production. As a result, the high probability of the ^{100}Mo (μ^-, n) ^{99}No reaction can be explained by the mean excitation energy.

Figure 5 shows the neutron spectrum for the ^{100}Mo (μ^-, xn) reaction. The curve is normalized arbitrarily. Since we do not consider the preequilibrium process, neutron spectra at higher excitation energies are considered to be strongly hindered. This anticipation is conceivable as one sees experimental data observed for muon capture reactions of other nuclei [56–58], in which neutron spectra at 40–50 MeV are only about 1/10 smaller than at 10 MeV. In addition, according to Ref. [15] (and reference therein), the contribution from the preequilibrium process to the primary neutron spectrum is approximately 13%. To reproduce the neutron spectrum, it is thus highly required to include the preequilibrium process in our framework.

From Table II, the rate of charged particle emission by ^{100}Mo (μ^-, x) is only 0.06%. The hindrance of the charged particle emissions is simply understood from the mean excitation energy. As seen in Fig. 4, the mean excitation energies are greater than S_p only for $0^{\pm}$, 1^+, 2^+, and 4^- states. Even though the excitation energies of those states are higher than S_p, the neutron emission occurs more easily than proton emission

TABLE III. Production of Nb isotopes by the muon capture reaction on Mo isotopes (%). Charged particle emission rates are also listed.

Reaction	This work
^{92}Mo $(\mu^-, 0n)$ ^{92}Nb	34.3
^{92}Mo $(\mu^-, 1n)$ ^{91}Nb	43.0
^{92}Mo $(\mu^-, 2n)$ ^{90}Nb	9.48
^{92}Mo $(\mu^-, 3n)$ ^{89}Nb	0.12
^{92}Mo $(\mu^-, 4n)$ ^{88}Nb	0.00
^{92}Mo $(\mu^-, 5n)$ ^{87}Nb	0.00
Charged particle emission	13.1
^{94}Mo $(\mu^-, 0n)$ ^{94}Nb	33.2
^{94}Mo $(\mu^-, 1n)$ ^{93}Nb	43.4
^{94}Mo $(\mu^-, 2n)$ ^{92}Nb	20.1
^{94}Mo $(\mu^-, 3n)$ ^{91}Nb	2.27
^{94}Mo $(\mu^-, 4n)$ ^{90}Nb	0.01
^{94}Mo $(\mu^-, 5n)$ ^{89}Nb	0.00
Charged particle emission	1.12
^{96}Mo $(\mu^-, 0n)$ ^{96}Nb	32.1
^{96}Mo $(\mu^-, 1n)$ ^{95}Nb	43.3
^{96}Mo $(\mu^-, 2n)$ ^{94}Nb	20.8
^{96}Mo $(\mu^-, 3n)$ ^{93}Nb	3.54
^{96}Mo $(\mu^-, 4n)$ ^{92}Nb	0.07
^{96}Mo $(\mu^-, 5n)$ ^{91}Nb	0.00
Charged particle emission	0.22
^{98}Mo $(\mu^-, 0n)$ ^{98}Nb	31.0
^{98}Mo $(\mu^-, 1n)$ ^{97}Nb	43.5
^{98}Mo $(\mu^-, 2n)$ ^{96}Nb	20.9
^{98}Mo $(\mu^-, 3n)$ ^{95}Nb	4.43
^{98}Mo $(\mu^-, 4n)$ ^{94}Nb	0.11
^{98}Mo $(\mu^-, 5n)$ ^{93}Nb	0.00
Charged particle emission	0.05

because S_n is 4 MeV lower than S_p. The emitted neutron withdraws energy and the compound nucleus is no longer able to emit protons. The Coulomb barrier also hinders the proton emission. For α-particle emission, $Q_\alpha \simeq 3.1$ MeV is lower than S_n. However, it has a larger Coulomb barrier than the proton, and transmission probability is thus expected to be small.

To conclude this subsection, the hindrance of the charged particle emission is discussed for Mo isotopes. Because ^{100}Mo is located in a relatively neutron-rich part of the nuclear chart, S_p is much higher than in other Mo isotopes. Therefore, the charged particle emission may occur at higher probability for Mo isotopes with smaller mass numbers than ^{100}Mo. To investigate them, we calculate the isotope production rates by the muon capture reaction on other Mo isotopes, and the results are shown in Table III. The reaction rates of (μ^-, xn) are similar to the ^{100}Mo case. In any isotope, one-neutron emission occurs at high probability as in the muon capture reaction on ^{100}Mo. In contrast, the charged particle emission rate for the muon capture reaction varies with respect to the mass number. With decreasing mass number, the charged particle emission rate becomes larger, since the neutron and proton separation energies are $S_n = 7.2$ and $S_p = 6.5$ MeV for ^{94}Nb, $S_n = 6.9$ and $S_p = 7.2$ MeV for ^{96}Nb, and $S_n = 6.0$ and $S_p = 7.9$ MeV for ^{98}Nb. Finally, the rate for ^{92}Nb gives a high probability of about 13%. This is because the proton separation energy of ^{92}Nb ($S_p = 5.8$ MeV) is lower than the neutron separation energy ($S_n = 7.9$ MeV), and thus the proton emission occurs much more easily in ^{92}Nb than in ^{100}Nb.

IV. SUMMARY

In order to understand the detailed mechanism of Nb isotope production through the muon capture reaction on ^{100}Mo, we studied the muon capture and subsequent particle evaporation with a microscopic theoretical model. We used the *pn*-QRPA on the basis of the SLy4 energy density functional for the muon capture and the Hauser-Feshbach statistical model for the particle evaporation process.

Our framework gives a reasonable agreement with the experimental data of the muon capture rate on $^{\text{nat}}$Mo. From the calculation, it is found that negative parity states populated by the muon capture on ^{100}Mo have a major contribution to the muon capture reaction at low excitation energy, while positive parity states have a major contribution at higher excitation energy. We demonstrated this difference by considering the nuclear shell structure of ^{100}Nb.

Our framework reasonably reproduced the experimentally measured Nb isotope production. A high probability of ^{100}Mo (μ^-, n) ^{99}Nb could be explained by the 1^- state populated by the muon capture, which has a large contribution to the muon capture reaction at excitation energies around S_n. This finding and the hindrance of charged particle emissions are also discussed qualitatively by using mean excitation energy.

While there are plenty of theoretical studies on charge-changing transitions, the β^+ transition extending to a high excitation energy region as a cause of negative muon capture is not well studied. In addition, the muon capture involves high multipole transitions, including natural and unnatural parities. To understand those physics, further effort is demanded from both experimental and theoretical sides, and the muon capture reaction, especially the isotope production rate, may provide us an important insight for improvement of theoretical models. In our theoretical framework, preequilibrium and direct processes are omitted. Those contributions would improve the results obtained in neutron spectra as well as isotope productions. We plan to include those contributions in our framework as a next development.

Finally, we roughly estimate the muon intensity, I_μ, to produce enough ^{99}Mo for diagnostics application. The activity of X Bq of ^{99}Mo after beam irradiation time t can be computed by $X = R[1 - \exp(-\lambda t)]$, where $R = I_\mu \omega_{fi}/(\omega_{fi} + H\omega_{\text{weak}}) P_{\text{Nb-99}}$ is the ^{99}Mo production rate by the muon reaction and λ is the decay constant of ^{99}Mo. Considering that the activity level demanded daily in the USA is $X = 81$ TBq (55.5 TBq in terms of ^{99m}Tc [59], where Ref. [60] is used for the conversion) and 24 h irradiation, the required muon beam intensity is $I_\mu \simeq 7.6 \times 10^{14}$ μ/s, where we use $\omega_{fi} = 8.34 \times 10^6$ s^{-1} (Sec. III A) and $P_{\text{Nb-99}} = 0.51$ [15] for the calculation. It is not easy to produce such a high

muon intensity using current accelerators and technology, and thus further developments are required to apply the muon reaction to ^{99}Mo production.

ACKNOWLEDGMENTS

The authors acknowledge S. Abe (JAEA) for his valuable cooperation concerning PHITS calculations. T.N. would like to thank the RIKEN iTHEMS program, the JSPS-NSFC Bilateral Program for Joint Research on Project on Nuclear mass and life for unravelling mysteries of the r process, and the JSPS Grant-in-Aid for JSPS Fellows under Grant No. 19J20543. Numerical calculations have been partially performed on cluster computers at the RIKEN iTHEMS program.

APPENDIX A: DERIVATION OF $V_{N\text{-}\mu}$

In this Appendix, the derivation of $V_{N\text{-}\mu}$ under the spherical-averaged charge distribution $\overline{\rho}_{\rm ch}$ is given. In the appendices, the dielectric constant of vacuum, ε_0, is shown explicitly.

According to the Maxwell equation [61], the charge distribution forms the electric field $\boldsymbol{E}_N$:

$$\varepsilon_0 \boldsymbol{E}_N(r) = e^2 \,\mathrm{div}\, \overline{\rho}_{\rm ch}(r), \tag{A1}$$

where $\boldsymbol{E}_N$ also holds the spherical symmetry. Equation (A1) can be rewritten as

$$4\pi r^2 E_N(r) = \frac{4\pi e^2}{\varepsilon_0} \int_0^r \overline{\rho}_{\rm ch}(r')\, r'^2\, dr'. \tag{A2}$$

Since a potential formed by $\overline{\rho}_{\rm ch}$ satisfies

$$E_N(r) = -\frac{dV_{N\text{-}\mu}(r)}{dr}, \tag{A3}$$

the potential reads

$$\begin{aligned} V_{N\text{-}\mu}(r) &= -\int_0^r E_N(r')\, dr' \\ &= -\frac{e^2}{\varepsilon_0} \int_0^r \frac{1}{r'^2} \int_0^{r'} \overline{\rho}_{\rm ch}(r'')\, r''^2\, dr''. \end{aligned} \tag{A4}$$

In the units we use in this paper $\varepsilon_0 = 1/4\pi$ holds and thus Eq. (7) is given.

APPENDIX B: CALCULABLE EXPRESSION $V_{e\text{-}\mu}$ UNDER THE SPHERICAL SYMMETRY

In this Appendix, an efficiently calculable form of Eq. (12) is given. The total charge inside the sphere with radius r due to ρ_e is written as

$$Q(r) = 4\pi e \int_0^r \rho_e(r)\, r^2\, dr, \tag{B1}$$

and the electric field formed by ρ_e at r is

$$E_e(r) = \frac{e}{4\pi\varepsilon_0} \frac{Q(r)}{r^2}. \tag{B2}$$

Therefore, the potential due to ρ_e is

$$\begin{aligned} V_{e\text{-}\mu}(r) &= e \int_r^\infty E_e(r')\, dr' \\ &= \frac{e^2}{4\pi\varepsilon_0} \int_r^\infty \frac{Q(r')}{r'^2}\, dr' \\ &= \frac{e^2}{4\pi\varepsilon_0} \int_r^\infty \left[\frac{d}{dr'}\left(-\frac{1}{r'}\right)\right] Q(r')\, dr' \\ &= \frac{e^2}{4\pi\varepsilon_0} \frac{Q(r)}{r} + \frac{e^2}{4\pi\varepsilon_0} \int_r^\infty \frac{1}{r'} \frac{dQ(r')}{dr'}\, dr' \\ &= \frac{e^2}{\varepsilon_0 r} \int_0^r \rho_e(r')\, r'^2\, dr' + \frac{e^2}{\varepsilon_0} \int_r^\infty \rho_e(r')\, r'\, dr'. \end{aligned} \tag{B3}$$

In the units we use in this paper $\varepsilon_0 = 1/4\pi$ holds and thus

$$V_{e\text{-}\mu}(r) = \frac{4\pi e^2}{r} \int_0^r \rho_e(r')\, r'^2\, dr' + 4\pi e^2 \int_r^\infty \rho_e(r')\, r'\, dr' \tag{B4}$$

is given.

Note that a similar calculation method is already used for the Hartree term in ADPACK [42].

[1] R. Van Noorden, Nature (London) **504**, 202 (2013).
[2] S. R. Cherry, J. A. Sorenson, and M. E. Phelps, *Physics in Nuclear Medicine* (Saunders, Philadelphia, 2003).
[3] R. G. Bennett, J. D. Christian, D. A. Petti, W. K. Terry, and S. B. Grover, Nucl. Technol. **126**, 102 (1999).
[4] A. V. Sabel'nikov, O. D. Maslov, L. G. Molokanova, M. V. Gustova, and S. N. Dmitriev, Radiochemistry **48**, 191 (2006).
[5] C. Ross, R. Galea, P. Saull *et al.*, Phys. Can. **66**, 19 (2010).
[6] H. Ejiri, T. Shima, S. Miyamoto, K. Horikawa, Y. Kitagawa, Y. Asano, S. Daté, and Y. Ohashi, J. Phys. Soc. Jpn. **80**, 094202 (2011).
[7] Y. Nagai and Y. Hatsukawa, J. Phys. Soc. Jpn. **78**, 033201 (2009).
[8] Y. Nagai, K. Hashimoto, Y. Hatsukawa, H. Saeki, S. Motoishi, N. Sato, M. Kawabata, H. Harada, T. Kin, K. Tsukada, T. K. Sato, F. Minato, O. Iwamoto, N. Iwamoto, Y. Seki, K. Yokoyama, T. Shiina, A. Ohta, N. Takeuchi, Y. Kawauchi, N. Sato, H. Yamabayashi, Y. Adachi, Y. Kikuchi, T. Mitsumoto, and T. Igarashi, J. Phys. Soc. Jpn. **82**, 064201 (2013).
[9] F. Minato, K. Tsukada, N. Sato, S. Watanabe, H. Saeki, M. Kawabata, S. Hashimoto, and Y. Nagai, J. Phys. Soc. Jpn. **86**, 114803 (2017).
[10] K. Tsukada, Y. Nagai, K. Hashimoto, M. Kawabata, F. Minato, H. Saeki, S. Motoishi, and M. Itoh, J. Phys. Soc. Jpn. **87**, 043201 (2018).
[11] K. Nagamine, *Introductory Muon Science* (Cambridge University Press, Cambridge, 2003).
[12] D. Duplain, B. Goulard, and J. Joseph, Phys. Rev. C **12**, 28 (1975).
[13] P. Christillin, A. Dellafiore, and M. Rosa-Clot, Nuovo Cimento A **34**, 289 (1976).
[14] N. Auerbach and A. Klein, Nucl. Phys. A **422**, 480 (1984).

[15] I. H. Hashim, H. Ejiri, T. Shima, K. Takahisa, A. Sato, Y. Kuno, K. Ninomiya, N. Kawamura, and Y. Miyake, Phys. Rev. C **97**, 014617 (2018).

[16] I. Hashim, H. Ejiri, F. Othman, F. Ibrahim, F. Soberi, N. Ghani, T. Shima, A. Sato, and K. Ninomiya, Nucl. Instrum. Methods Phys. Res., Sect. A **963**, 163749 (2020).

[17] H. Ejiri, I. H. Hashim, Y. Hino, Y. Kuno, Y. Matsumoto, K. Ninomiya, H. Sakamoto, A. Sato, T. Shima, A. Shinohara, K. Takahisa, and N. H. Tran, J. Phys. Soc. Jpn. **82**, 044202 (2013).

[18] H. Ejiri and M. J. A. de Voight, *Gamma Ray and Electron Spectroscopy in Nuclear Physics* (Oxford University Press, Oxford, 1989).

[19] L. Jokiniemi, J. Suhonen, H. Ejiri, and I. Hashim, Phys. Lett. B **794**, 143 (2019).

[20] D. Vautherin, Phys. Rev. C **7**, 296 (1973).

[21] W. Hauser and H. Feshbach, Phys. Rev. **87**, 366 (1952).

[22] E. Kolbe, K. Langanke, and P. Vogel, Phys. Rev. C **50**, 2576 (1994).

[23] E. Kolbe, K. Langanke, and P. Vogel, Phys. Rev. C **62**, 055502 (2000).

[24] N. T. Zinner, K. Langanke, and P. Vogel, Phys. Rev. C **74**, 024326 (2006).

[25] T. Marketin, N. Paar, T. Nikšić, and D. Vretenar, Phys. Rev. C **79**, 054323 (2009).

[26] V. W. Hughes and C. Wu (eds.), *Muon Physics* (Academic, New York, 1975).

[27] J. S. O'Connell, T. W. Donnelly, and J. D. Walecka, Phys. Rev. C **6**, 719 (1972).

[28] E. Tiesinga, P. J. Mohr, D. B. Newell, and B. N. Taylor, The 2018 CODATA Recommended Values of the Fundamental Physical Constants (Web Version 8.0), http://physics.nist.gov/constants, 2019, mD 20899.

[29] J. Engel, M. Bender, J. Dobaczewski, W. Nazarewicz, and R. Surman, Phys. Rev. C **60**, 014302 (1999).

[30] P. Ring and P. Schuck, *The Nuclear Many-Body Problem* (Springer-Verlag, Berlin, 1980).

[31] E. Chabanat, P. Bonche, P. Haensel, J. Meyer, and R. Schaeffer, Nucl. Phys. A **635**, 231 (1998).

[32] P.-G. Reinhard, D. J. Dean, W. Nazarewicz, J. Dobaczewski, J. A. Maruhn, and M. R. Strayer, Phys. Rev. C **60**, 014316 (1999).

[33] N. Van Giai and H. Sagawa, Phys. Lett. B **106**, 379 (1981).

[34] M. Bender, J. Dobaczewski, J. Engel, and W. Nazarewicz, Phys. Rev. C **65**, 054322 (2002).

[35] C. L. Bai, H. Q. Zhang, H. Sagawa, X. Z. Zhang, G. Colò, and F. R. Xu, Phys. Rev. C **83**, 054316 (2011).

[36] X. Roca-Maza, G. Colò, and H. Sagawa, Phys. Rev. C **86**, 031306(R) (2012).

[37] M. T. Mustonen, T. Shafer, Z. Zenginerler, and J. Engel, Phys. Rev. C **90**, 024308 (2014).

[38] H. De Vries, C. De Jager, and C. De Vries, At. Data Nucl. Data Tables **36**, 495 (1987).

[39] P. Hohenberg and W. Kohn, Phys. Rev. **136**, B864 (1964).

[40] W. Kohn and L. J. Sham, Phys. Rev. **140**, A1133 (1965).

[41] A. H. MacDonald and S. H. Vosko, J. Phys. C **12**, 2977 (1979).

[42] T. Ozaki, H. Kino, H. Kawai, and M. Toyoda, ADPACK Ver. 2.2, http://www.openmx-square.org/adpack_man2.2/ (2011).

[43] J. P. Perdew and A. Zunger, Phys. Rev. B **23**, 5048 (1981).

[44] O. Iwamoto, N. Iwamoto, S. Kunieda, F. Minato, and K. Shibata, Nucl. Data Sheets **131**, 259 (2016).

[45] A. Koning and J. Delaroche, Nucl. Phys. A **713**, 231 (2003).

[46] M. Avrigeanu and V. Avrigeanu, Phys. Rev. C **82**, 014606 (2010).

[47] J. Kopecky and M. Uhl, Phys. Rev. C **41**, 1941 (1990).

[48] A. Gilbert and A. G. W. Cameron, Can. J. Phys. **43**, 1446 (1965).

[49] A. Mengoni and Y. Nakajima, J. Nucl. Sci. Technol. **31**, 151 (1994).

[50] W. Huang, G. Audi, M. Wang, F. G. Kondev, S. Naimi, and X. Xu, Chin. Phys. C **41**, 030002 (2017).

[51] M. Wang, G. Audi, F. G. Kondev, W. Huang, S. Naimi, and X. Xu, Chin. Phys. C **41**, 030003 (2017).

[52] P. Möller, W. D. Myers, H. Sagawa, and S. Yoshida, Phys. Rev. Lett. **108**, 052501 (2012).

[53] M. Lifshitz and P. Singer, Phys. Rev. C **22**, 2135 (1980).

[54] T. Suzuki, D. F. Measday, and J. P. Roalsvig, Phys. Rev. C **35**, 2212 (1987).

[55] M. Tanabashi, K. Hagiwara, K. Hikasa, K. Nakamura, Y. Sumino, F. Takahashi, J. Tanaka, K. Agashe, G. Aielli, C. Amsler, M. Antonelli, D. M. Asner, H. Baer, S. Banerjee, R. M. Barnett, T. Basaglia, C. W. Bauer, J. J. Beatty, V. I. Belousov, J. Beringer *et al.* (Particle Data Group), Phys. Rev. D **98**, 030001 (2018).

[56] V. Evseyev, T. Kozlowski, V. Roganov, and J. Wojtkowska, Phys. Lett. B **28**, 553 (1969).

[57] R. M. Sundelin and R. M. Edelstein, Phys. Rev. C **7**, 1037 (1973).

[58] T. Kozlowski, W. Bertl, H. Povel, U. sennhauser, H. Walter, A. Zglinski, R. Engfer, C. Grab, E. Hermes, H. Isaak, A. V. D. Schaaf, J. V. D. Pluym, and W. Hesselink, Nucl. Phys. A **436**, 717 (1985).

[59] M. R. A. Pillai, A. Dash, and F. F. R. Knapp, Jr., J. Nucl. Med. **56**, 159 (2015).

[60] R. Boyd, Int. J. Appl. Radiat. **33**, 801 (1982).

[61] W. Greiner, *Classical Electrodynamics* (Springer-Verlag, New York, 1998).